Chemical Engineering Journal 430 (2022) 132813

Contents lists available at ScienceDirect

Chemical Engineering Journal

journal homepage: www.elsevier.com/locate/cej

Room temperature WO_3-Bi_2WO_6 sensors based on hierarchical microflowers for ppb-level H_2S detection

Chao Zhang [a,*], Kaidi Wu [a,c], Hanlin Liao [b], Marc Debliquy [c]

[a] College of Mechanical Engineering, Yangzhou University, Yangzhou 225127, PR China
[b] ICB UMR 6303, CNRS, Univ. Bourgogne Franche-Comté, UTBM, 90010, Belfort, France
[c] Service de Science des Matériaux, Faculté Polytechnique, Université de Mons, Mons 7000, Belgium

ARTICLE INFO

Keywords:
WO_3-Bi_2WO_6
Hierarchical microflowers
Heterojunction
Gas sensor
H_2S

ABSTRACT

Pristine Bi_2WO_6 nanosheets and hierarchical WO_3-Bi_2WO_6 microflowers were prepared via a facile hydrothermal technique. WO_3-Bi_2WO_6 microflowers were assembled with thin nanosheets, where WO_3 nanoparticles were uniformly loaded. The H_2S sensing properties of pristine Bi_2WO_6 nanosheets and hierarchical WO_3-Bi_2WO_6 microflowers were systematically investigated at room temperature. 20 WO_3-Bi_2WO_6 microflowers sensor displayed the best sensing property towards ppb-level H_2S compared with all other samples. The enhancement was ascribed to the catalytic effect of WO_3 nanoparticles and the modified microstructure with large specific surface areas. Moreover, the n–n heterojunction structures also increase the thickness of electron depletion layer and potential barrier height, which could efficiently improve the sensing properties. The practical application of 20 WO_3-Bi_2WO_6 microflowers sensor in detecting the volatiles of Pangasius was also studied in this work. Therefore, the hierarchical WO_3-Bi_2WO_6 microflower is a promising ppb-level H_2S sensing material for environment monitoring and fish freshness detection.

1. Introduction

Environment and food safety have attracted more attention along with people's pursuit of healthy life [1,2]. Hydrogen sulfide (H_2S) is colorless, malodorous and toxic [3–5]. It shows a great threat to human health, which will stimulate and damage respiratory organs and eyes even at a low concentration. The threshold limit value (TLV) of H_2S for the industrial environment is defined as 10 ppm. Moreover, the acceptable level of the H_2S for a human health condition should not exceed 100 ppb [6]. H_2S is also a volatile biomarker gas resulting from the decomposition of sulfhydryl-containing amino acids in fish. The H_2S trace amounts will reach or even exceed ppb levels when fish starts spoiling [7]. Additionally, the variation of H_2S concentration (commonly in ppb level) in human exhaled breath can be utilized for diagnosing halitosis and real-time prevention of systemic diseases [8]. Hence, the development of high-performance gas sensing material for real-time and efficient ppb-level H_2S detection is necessary for the environment, food safety and human health.

Metal oxides semiconductor materials have been comprehensively investigated as gas-sensitive materials, due to their high sensitivity, low cost and easy integration. There have been a series of metal oxide nanomaterials for H_2S detection. Deng et al. reported a microwave-assisted hydrothermal synthesized porous α-Fe_2O_3 spheres based H_2S sensor, showing a fast response to H_2S with fine selectivity at 350 °C [9]. Peng et al. reported a CuO nanoparticles gas sensor, showing a response towards H_2S at 150 °C [10]. Wang et al. obtained ZnO microspheres assembled with nanosheets, and the corresponding sensor exhibited responses to 5–100 ppm H_2S at 70 °C [11]. Mokoena et al. prepared a non-stoichiometric NiO based H_2S sensor, which displayed good sensing performance in dry air at 75 °C [12]. Although the single metal oxide shows good sensing properties, the high operating temperature and detection threshold limitation affect the performance stability and practical application. Several strategies have been explored to lower the operating temperature and to improve the gas molecules' adsorption capacity, for instance, constructing unique hierarchical nanostructure, doping low amount of elements, loading on low-dimensional materials and fabricating homo or hetero-junction structures [13–17]. The results revealed that mixed binary metal oxides-based gas sensing materials obtained a significant improvement in both physical and chemical properties. Hence, binary metal oxide semiconductors have become emerging gas sensing materials, such as $ZnFe_2O_4$ [18] and $BiVO_4$ [19]. However, researchers seldom report room temperature bismuth

* Corresponding author.
E-mail address: zhangc@yzu.edu.cn (C. Zhang).

https://doi.org/10.1016/j.cej.2021.132813
Received 6 July 2021; Received in revised form 19 September 2021; Accepted 3 October 2021
Available online 5 October 2021

tungstate (Bi_2WO_6) gas sensors [20].

Bi_2WO_6, as a typical Aurivillius-phase perovskite, possesses a sandwich structure composed of perovskite layers $(WO_4)^{2-}$ and $(Bi_2O_2)^{2+}$ layers. Additionally, Bi_2WO_6 belongs to the n-type semiconductor with a bandgap of ~ 2.89 eV, which has been successfully used as a photocatalyst due to its outstanding electron transfer properties and excellent photo absorption capacity [21,22]. However, there are few reports about Bi_2WO_6 based gas sensors. Liu et al. synthesized a multilayer Bi_2WO_6 micro-nano hierarchical structure via template-assisted hydrothermal method, and the sensor showed a response and high selectivity towards ppm level H_2S at 260 °C, which was ascribed to the existence of oxygen vacancies, the high specific surface areas and large pore volume [23]. The Bi_2WO_6-rGO gas sensor showed fine sensing performance to 250 ppb H_2S at 350 °C, which benefited from the p-n heterojunctions between Bi_2WO_6 with well-dispersed rGO [24]. It is obvious that their operating temperatures were still high, as well as a little poor ppb-level H_2S sensing properties. Hence, it is urged to develop novel micro-nano structured Bi_2WO_6 based sensing materials for low temperature and high-performance detection.

In this work, we used a facile hydrothermal method with sodium dodecylbenzene sulfonate (SDBS) as an anionic surfactant to prepare Bi_2WO_6 hierarchical microflowers, and WO_3 nanoparticles were decorated on Bi_2WO_6 hierarchical microflowers. The characterization results showed WO_3 nanoparticles can be loaded on the Bi_2WO_6 hierarchical microflowers assembled with nanosheets without any post-treatment. The room temperature sensing properties towards ppb level H_2S were investigated. The observed improvement in sensing properties was ascribed to the hierarchical structure and n-n heterojunction structure of WO_3-Bi_2WO_6.

2. Material and methods

2.1. Synthesis of Bi_2WO_6 nanosheets and hierarchical WO_3-Bi_2WO_6 microflowers

All reagents (Shanghai Aladdin Biochemical Technology Co., Ltd.) were purchased as analytical grade reagents without further purification. Bi_2WO_6 nanosheets and hierarchical WO_3-Bi_2WO_6 microflowers decorated with different mass fractions of WO_3 nanoparticles were synthesized. Bi_2WO_6 nanosheets are prepared via a hydrothermal method starting from $Bi(NO_3)_3{\cdot}5H_2O$ and $Na_2WO_4{\cdot}2H_2O$ as precursors. The principle of the decoration is to add an excess of WO_3 precursor (In this case, $Na_2WO_4{\cdot}2H_2O$) during the formation of the Bi_2WO_6 nanosheets via the following procedure: 0.97 g $Bi(NO_3)_3{\cdot}5H_2O$, certain amounts of $Na_2WO_4{\cdot}2H_2O$ (ranging from 0.33 g to 0.99 g), and 0.0348 g SDBS were mixed into 35 mL deionized water, subsequently transferred the obtained suspension to 50 mL Teflon-lined stainless autoclaves after magnetically stirred for 1 h. It was then maintained at 180 °C for 24 h and cooled down naturally. These products were centrifuged with absolute ethanol 5 times. Finally, a series of as-synthesized samples were obtained after a drying treatment at 80 °C for 6 h in an oven. The final products synthesized with $Na_2WO_4{\cdot}2H_2O$ of 0.33 g, 0.495 g (10 wt%), 0.66 g (20 wt%), 0.824 g (30 wt%) and 0.99 g (40 wt%) are denoted as Bi_2WO_6, 10 WO_3-Bi_2WO_6, 20 WO_3-Bi_2WO_6, 30 WO_3-Bi_2WO_6 and 40 WO_3-Bi_2WO_6.

2.2. Characterization

The phase structures of all powders were determined via X-ray diffraction (XRD) using Cu-K_α radiation with a scanning rate of $5^\circ{\cdot}min^{-1}$ (D8 Advance Bruker). The morphological characteristics and elements distribution of Bi_2WO_6 were inspected using field-emission scanning electron microscopy (FESEM, S4800II Hitachi) equipped with energy-dispersive X-ray spectroscopy. The further nanostructure of products was observed by transmission electron microscopy (TEM, JEM-2100). High-resolution TEM (HRTEM) information was obtained using field emission transmission electron microscopy (Tecnai G2 F30 S-TWIN, FEI). The chemical states of the elements were also studied by X-ray photoelectron spectroscopy (XPS, Thermo Fisher Scientific ESCALAB 250Xi). The BET specific surface areas were acquired through N_2 adsorption/ desorption at 77 K. The pore sizes of samples were calculated by Barret-Joyner-Halenda (BJH) method using the isotherms (Autosorb IQ3, Quantachrome Instruments).

2.3. Fabrication and measurement of gas sensors

As shown in Fig. S1, the electrode slice was prepared based on the alumina substrate (6*30 mm). The platinum paste was printed by screen printing onto the alumina substrates. The alumina substrates were calcined at 350 °C and then 850 °C for 20 min successively after being dried for 30 min at 80 °C. The Pt layer was composed of a heating element and measuring electrodes. The as-synthesized powders (~3 mg) were firstly mixed with deionized water (~1 mL) to obtain a slurry via using mortar and pestle, which was then brushed uniformly on the upper side of alumina substrate equipped with Pt electrodes on the same side. The gas sensor was obtained after drying and treatment at 150 °C for 12 h. The gas sensor test was carried out by a four-channel gas sensing testing instrument (Wuhan Huachuang Ruike Technology Co., Ltd.), which can collect electrical resistance signals of the corresponding channel with a DC power supply of 12 V and 4 A. The gas sensing tests were performed at room temperature (20 ± 2 °C) and the relative humidity RH is around 30 %. The other details of the testing system are displayed in Fig. S1.

The responses of n-type Bi_2WO_6 and WO_3-Bi_2WO_6 are defined as R_a/R_g, which is the ratio of the stable sensor resistance in air to the stable sensor resistance in target gas. The response/recovery time is taken from the time for achieving 90 % change of resistance values.

The fish freshness detection is measured on a homemade testing system. As shown in Fig. S2, 10 g fresh Pangasius fillet purchased from a local supermarket was firstly defrosted and then placed in a 1.25 L closed scrubber at ambient conditions and detected the released H_2S over different storage periods (0, 1, 2, 3, 4, 5, 12 and 24 h).

3. Results and discussion

3.1. Characterization results

XRD patterns of all samples from 10° to 80° are displayed in Fig. 1a. These distinct diffraction peaks observed at around 28.31°, 32.79°, 47.16°, 55.98°, 58.61°, 69.19°, 76.20°, 78.39° and 87.64° are attributed to the standard orthorhombic-phase structure of Bi_2WO_6 (JCPDS No. 39–0256). As the dopant amounts of WO_3 nanoparticles increased, there exist obvious intensified monoclinic WO_3 diffraction peaks at around 23.08° (JCPDS No. 43–1035), and the peak intensity of Bi_2WO_6 decreased compared with pure Bi_2WO_6. The average crystal sizes of all samples are estimated using the Debye-Scherrer formula: $D = 0.89\lambda/(\beta \cos\theta)$, where $\lambda = 0.15406$ nm, β is the full width at half maximum and θ is the diffraction angle of the peaks. The crystal sizes of Bi_2WO_6, 10 WO_3-Bi_2WO_6, 20 WO_3-Bi_2WO_6, 30 WO_3-Bi_2WO_6 and 40 WO_3-Bi_2WO_6 are estimated to be 8.1, 11.6, 12.6, 8.5 and 8.7 nm, respectively. Besides, there are no extra obvious peaks, which implies the obtained WO_3-Bi_2WO_6 composites possess perfect phase structure and high purity.

The morphologies of all samples were observed through FESEM and TEM. In Fig. 1b and 1c, the FESEM images indicate that pure Bi_2WO_6 products mainly consist of numerous nanosheets. In Fig. S3a and Fig. S3b, 10 WO_3-Bi_2WO_6 showed microflowers with a diameter of around 2 μm were assembled with thin nanosheets. The high magnification image demonstrated that there were amounts of WO_3 nanoparticles loaded on the surface of microflowers. As the dopant amounts of WO_3 nanoparticles continue to increase, it is interesting to observe that 20 WO_3-Bi_2WO_6 sample showed the hierarchical microflowers decorated with nanoparticles in Fig. 1d and 1e. 30 WO_3-Bi_2WO_6 and 40

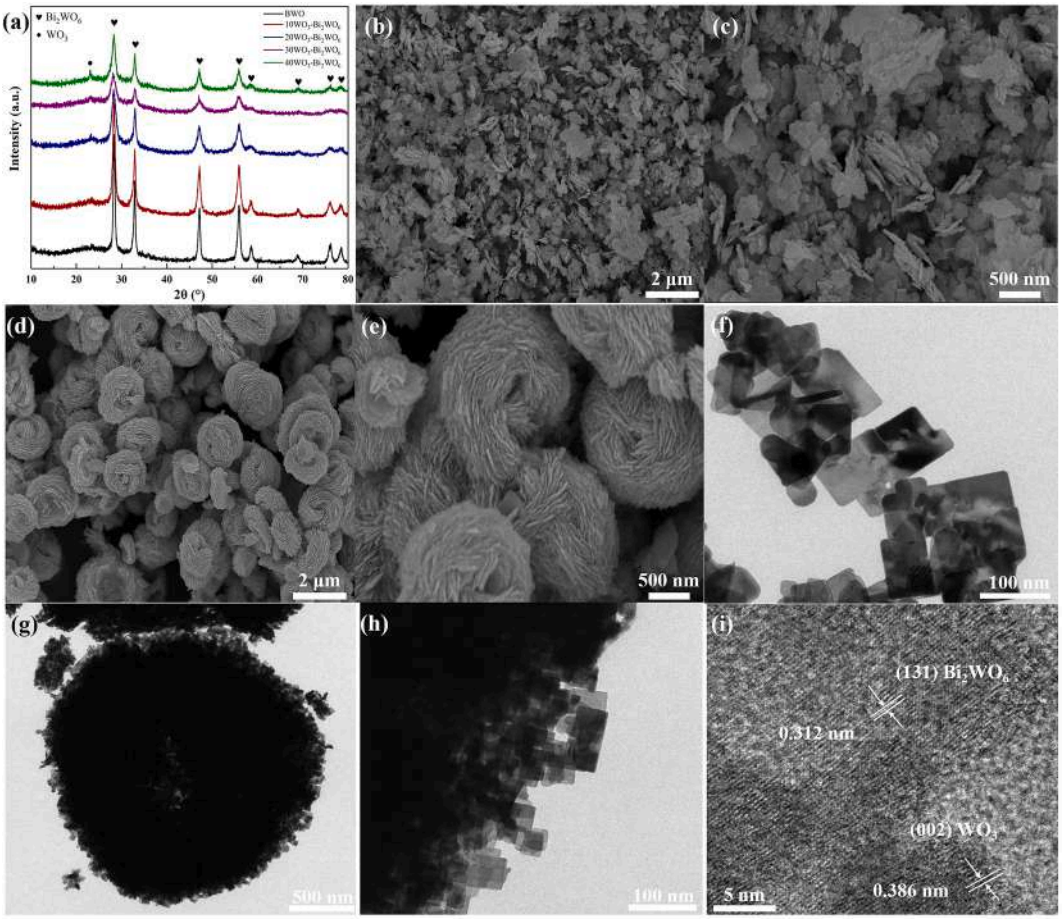

Fig. 1. (a) XRD patterns of pristine Bi_2WO_6 and WO_3-Bi_2WO_6 composites; FESEM images of (b, c) pristine Bi_2WO_6 and (d, e) 20 WO_3-Bi_2WO_6; TEM images of (f) pristine Bi_2WO_6, (g, h) 20 WO_3-Bi_2WO_6, (i) HR-TEM image of 20 WO_3-Bi_2WO_6.

WO_3-Bi_2WO_6 were displayed in Fig. S3(c–f). There is no difference in the average diameter of microflowers whereas the nanoparticles decorated on the surface became denser when the contents of WO_3 exceeded 20 wt %, which may affect their gas sensing properties. Additionally, Fig. S4 showed the elemental mapping results of 20 WO_3-Bi_2WO_6 microspheres, and all the elements are observed to be distributed uniformly.

As shown in Fig. 1(f and g), TEM analysis further confirms the microstructure of pure Bi_2WO_6 and WO_3-Bi_2WO_6. In Fig. 1f, pure Bi_2WO_6 displays that thin nanosheets stacked on each other. Fig. 1g and 1 h reveal the nanosheets assembled spherical and hollow microstructure of 20 WO_3-Bi_2WO_6, which can afford enough active sites for gas adsorption, as well as surface regions for gas-solid phase reaction [25]. In addition, the morphologies and sizes of hierarchical 20 WO_3-Bi_2WO_6 microflowers are consistent with the observed FESEM images. As shown in Fig. 1i, the HRTEM image of 20 WO_3-Bi_2WO_6 further confirms the phase composition. The crystalline interplanar spacing of 0.312 nm and 0.386 nm are indexed to the (1 3 1) plane of Bi_2WO_6 and (0 0 2) plane of WO_3, respectively.

According to the observation results of phase structure, morphology, and nanostructure, the synthesis mechanism of the hierarchical WO_3-

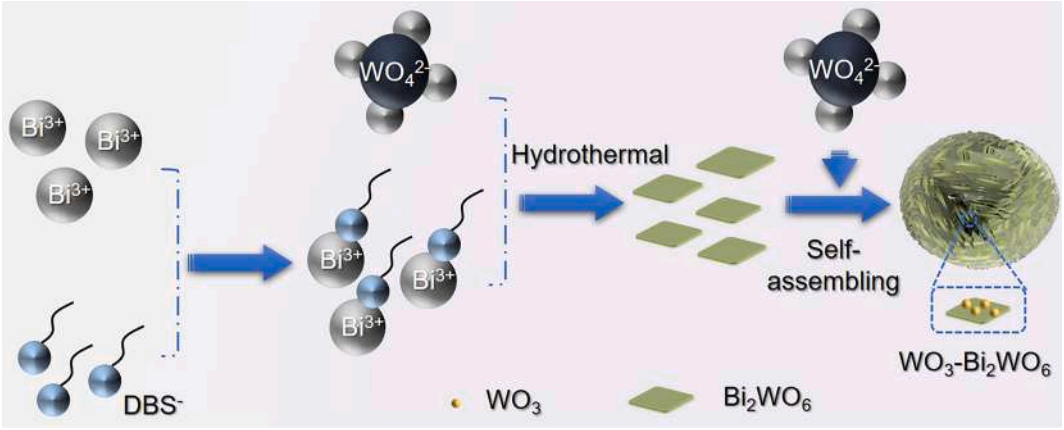

Scheme 1. Synthesis mechanism of pristine Bi_2WO_6 and WO_3-Bi_2WO_6.

Bi_2WO_6 microflowers is proposed in Scheme 1. Bi^{3+} cations and DBS^- anions are firstly bonded together to form Bi-DBS complexes resulting from the electrostatic interactions, which contributes to hindering the hydrolysis of $Bi^{3+}$and dispersion in the solution. With the introduction of WO_4^{2-}, it reacts with Bi-DBS to generate Bi_2WO_6 nanosheets. Once the molar ratio of W to Bi element exceeds 1:2, WO_3 nanoparticles will be generated and deposited on Bi_2WO_6 nanosheets. Subsequently, they will self-assemble into WO_3-Bi_2WO_6 hierarchical microflowers for reducing the surface energy [26,27].

The element chemical states of pristine Bi_2WO_6 and 20 WO_3-Bi_2WO_6 were inspected by XPS. In Fig. 2a, the full survey XPS spectra of the two samples reveal that the four elements, Bi, W, O and C exist in both obtained products. Notably, C 1 s peak was used as the reference for energy calibration in XPS measurements. Fig. 2b displayed two fitted peaks located at 163.95 and 158.63 eV in pure Bi_2WO_6 spectra, corresponding to Bi 4f5/2 and Bi 4f7/2, respectively. Meanwhile, there are also two similar characteristic peaks of 20 WO_3-Bi_2WO_6, demonstrating the existence of Bi^{3+} in the products [28]. Fig. 2c displayed the high-resolution XPS spectrum of W 4f, which is fitted into two peaks of W 4f5/2 at 36.98 eV and W 4f7/2 at 34.83 eV, suggesting the presence of W^{6+} in the pristine sample [29]. As for 20 WO_3-Bi_2WO_6, the characteristic spin–orbit peaks of Bi 4f and W 4f both displayed a slight shift to the high binding energy (Bi 4f: 0.23 and 0.26 eV; Bi 4f: 0.27 and 0.28 eV), which may be attributed to the influence of WO_3 nanoparticles on the chemical environment of Bi and W [30]. Fig. 2d presents the O 1 s spectra, which can be resolved into three peaks. The two peaks located at the binding energy of 529.51 eV and 530.53 eV correspond to the lattice oxygen, while the peak at 531.48 eV is attributed to the adsorbed oxygen species [31]. As for 20 WO_3-Bi_2WO_6, there are three fitted peaks at the higher binding energy of 529.86, 530.55, and 531.78 eV. The shift to the higher binding energy of O 1 s peaks (0.35, 0.02, and 0.30 eV) may be ascribed to the reduction of the electron density around oxygen atoms, resulting from the formation of heterojunction in WO_3-Bi_2WO_6 composites [32,33]. Moreover, the intensity ratio of W-O to Bi-O peaks in WO_3-Bi_2WO_6 significantly increases compared with the pristine Bi_2WO_6, which also demonstrates the successful introduction of WO_3 into the composite. All the above results confirm the existence of n-n heterojunction in hierarchical 20 WO_3-Bi_2WO_6 microflowers.

The BET surface area of Bi_2WO_6 and 20 WO_3-Bi_2WO_6 samples were also obtained via the nitrogen adsorption–desorption isothermal technique. The isotherms plot of Bi_2WO_6 nanosheets and 20 WO_3-Bi_2WO_6 microflowers are displayed in Fig. 3. According to the isotherms and average pores diameters of Bi_2WO_6 nanosheets and 20 WO_3-Bi_2WO_6 microflowers, they all exhibit mesoporous structures [29]. The specific surface areas of Bi_2WO_6 nanosheets and 20 WO_3-Bi_2WO_6 microflowers were 22.7 $m^2 \cdot g^{-1}$ and 47.5 $m^2 \cdot g^{-1}$, respectively. The results indicate that the microstructures and surface characteristics were modified after introducing WO_3 nanoparticles. Moreover, the hierarchical structures with large surface area and porous structures are in favor of gas molecules' adsorption and transportation, which results in improving the sensing properties of 20 WO_3-Bi_2WO_6. In addition, Figure S5 showed the N_2 adsorption–desorption isothermal plots of 10, 30 and 40 WO_3-Bi_2WO_6 composites. And as shown in Table S1, the specific surface areas of 10, 30 and 40 WO_3-Bi_2WO_6 were 25.4, 52.4 and 42.8 $m^2 \cdot g^{-1}$, respectively. The WO_3 nanoparticles improve the specific surface areas, especially the WO_3 amounts of 20, 30 and 40, which will provide more active sites for gas molecules adsorption and reaction. In Table S1, the average pore diameters of x wt% WO_3-Bi_2WO_6 (x = 0, 10, 20, 30 and 40) composites were 37.1 nm, 18.2 nm, 14.1 nm, 9.1 nm and 18.0 nm, respectively. And the corresponding total pore volumes are 0.192, 0.116, 0.168, 0.119 and 0.193 $cm^3 \cdot g^{-1}$, respectively.

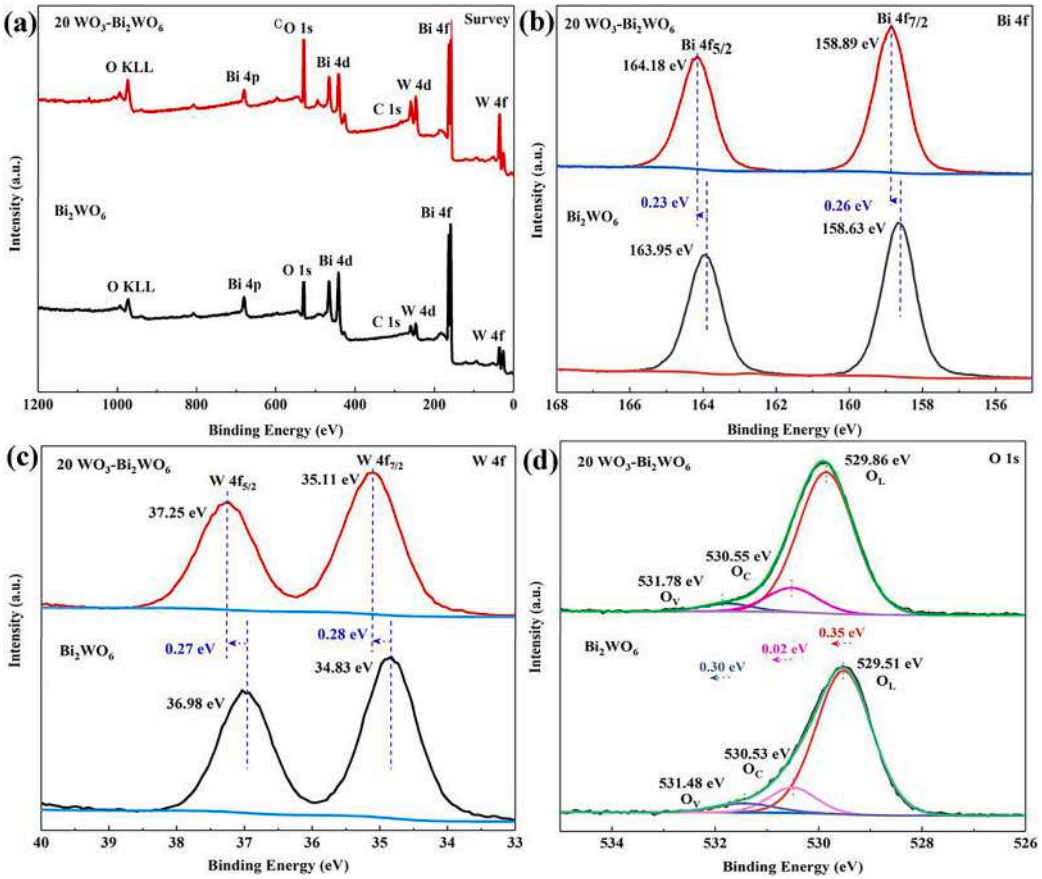

Fig. 2. Elements chemical states of pristine Bi_2WO_6 and 20 WO_3-Bi_2WO_6 composite determined by XPS: (a) survey, (b) Bi 4f, (c) W 4f and (d) O 1 s.

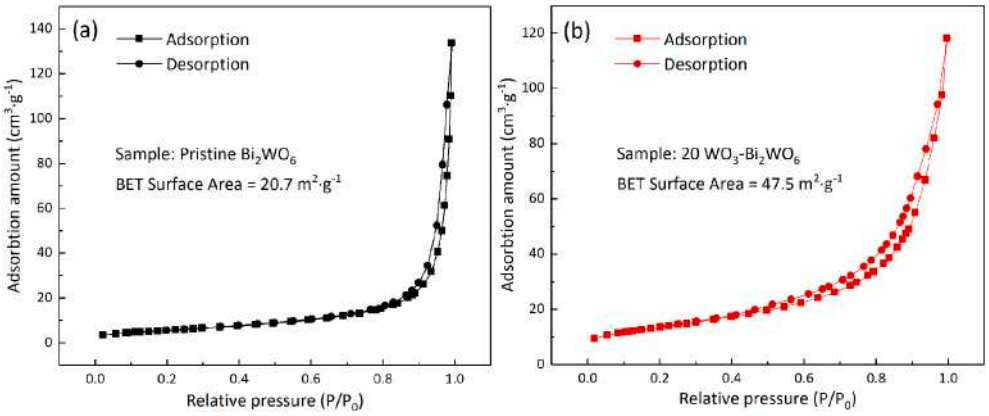

Fig. 3. Nitrogen adsorption–desorption measurement isotherm of (a) pristine Bi_2WO_6 and (b) 20 WO_3-Bi_2WO_6 composite.

3.2. Room temperature gas sensing performance

The sensing properties of Bi_2WO_6 nanosheets and hierarchical WO_3-Bi_2WO_6 microflowers composites were evaluated at room temperature. The role of dopant amounts of WO_3 nanoparticles on hierarchical Bi_2WO_6 microflowers gas sensors was first investigated. Fig. 4a depicted that there is no response of pristine Bi_2WO_6 nanosheets and 10 WO_3-Bi_2WO_6 towards 50 ppb H_2S, while 20/30/40 WO_3-Bi_2WO_6 composites showed fine responses to ppb-level H_2S. Notably, the response of 20 WO_3-Bi_2WO_6 was 4.4, which was much higher than those of 30 and 40 WO_3-Bi_2WO_6. Furthermore, the response/recovery speed of three WO_3-Bi_2WO_6 was also measured at the same conditions. Among them, 20 WO_3-Bi_2WO_6 exhibited the shortest response/recovery time (52 s/119 s) to 50 ppb H_2S at room temperature. The introduction amounts of WO_3 nanoparticles play a key role in the sensing properties of WO_3-Bi_2WO_6 composites. Hence, 20 WO_3-Bi_2WO_6 was chosen as the best H_2S sensing material.

To further understand the dynamic response behavior of WO_3-Bi_2WO_6, Fig. 5a and 5b display the transient response/recovery curves of 20 WO_3-Bi_2WO_6, 30 WO_3-Bi_2WO_6 and 40 WO_3-Bi_2WO_6 to 2–50 ppb H_2S at room temperature. 20 WO_3-Bi_2WO_6 showed a much higher response than those of 30 WO_3-Bi_2WO_6 and 40 WO_3-Bi_2WO_6, revealing that the response of Bi_2WO_6 based composite to H_2S was significantly improved via compounding with 20 wt% WO_3 nanoparticles. 20 WO_3-Bi_2WO_6 showed a large sensing capacity to ppb-level H_2S, and it can detect 2 ppb H_2S with a response of 1.13. In Fig. 5c, the fitting curves of two WO_3-Bi_2WO_6 samples fitted a linear relationship between response values and H_2S concentration. Moreover, these linear fitting curves showed that the correlation coefficients R^2 were in the range of ~ 0.974–0.998, and 20 WO_3-Bi_2WO_6 present the highest correlation coefficient. Additionally, the theoretical limit of detection (LOD) was calculated from the experimental and fitting data by using the following equation [18]:

$$D_L = 3(RMS_{noise}/k)$$

in which RMS_{noise} is the gas sensor noise calculated via root-mean-square deviation processing on the stable baseline data taken exposure to air in Fig. 5f, k is the values of the slope of corresponding linear fitting curves. As shown in Table S2, the theoretical LOD of all three gas sensors are around 2 ppb, 8 ppb and 7 ppb, respectively.

For monitoring the environment or freshness detection practically, selectivity as an important sensing characteristic should be evaluated. In Fig. 5d, 20 WO_3-Bi_2WO_6 sensor was investigated using four interfering gases including NH_3, SO_2, CO and H_2 of 100 ppb at the same condition. The response value was 7.86 towards H_2S, while the responses to SO_2, NH_3, CO and H_2 were around 1.86, 1.11, 1.16 and 1.15, respectively. It can be concluded that the 20 WO_3-Bi_2WO_6 microflowers sensor has an excellent selectivity, which is mainly attributed to two aspects. First, due to the lower bond dissociation energy of H-S in H_2S molecules compared to other target gases, it can be easily broken and interact with surface chemisorbed oxygen ions [34]. Second, the formation of n-n heterojunction at the interfaces of WO_3 and Bi_2WO_6 is also favorable for H_2S oxidation on the surface [35]. The humidity effect of 20 WO_3-Bi_2WO_6 microflowers sensor under a relative humidity of 30%, 50% and 70%

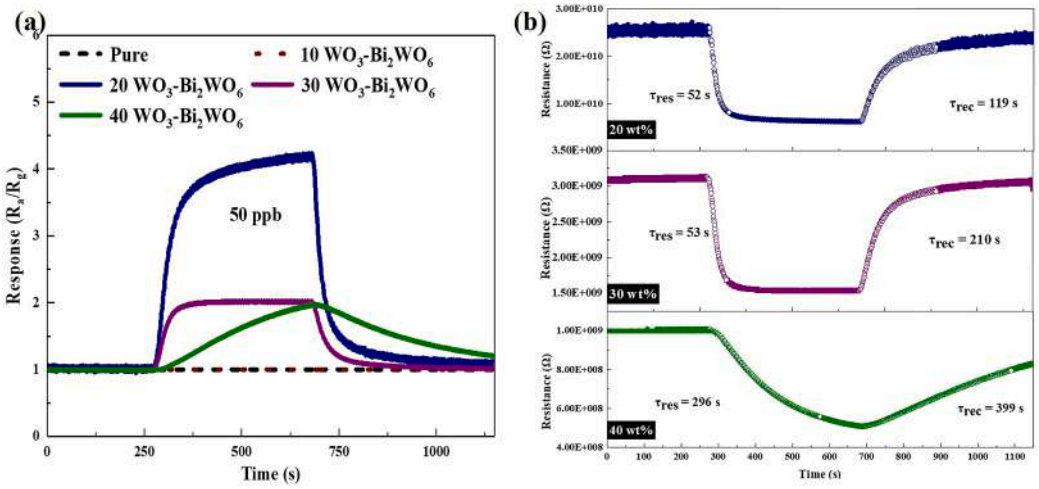

Fig. 4. (a) Responses to 50 ppb H_2S at room temperature; (b) dynamic response/recovery curves of 20 WO_3-Bi_2WO_6, 30 WO_3-Bi_2WO_6 and 40 WO_3-Bi_2WO_6 to 50 ppb H_2S at room temperature.

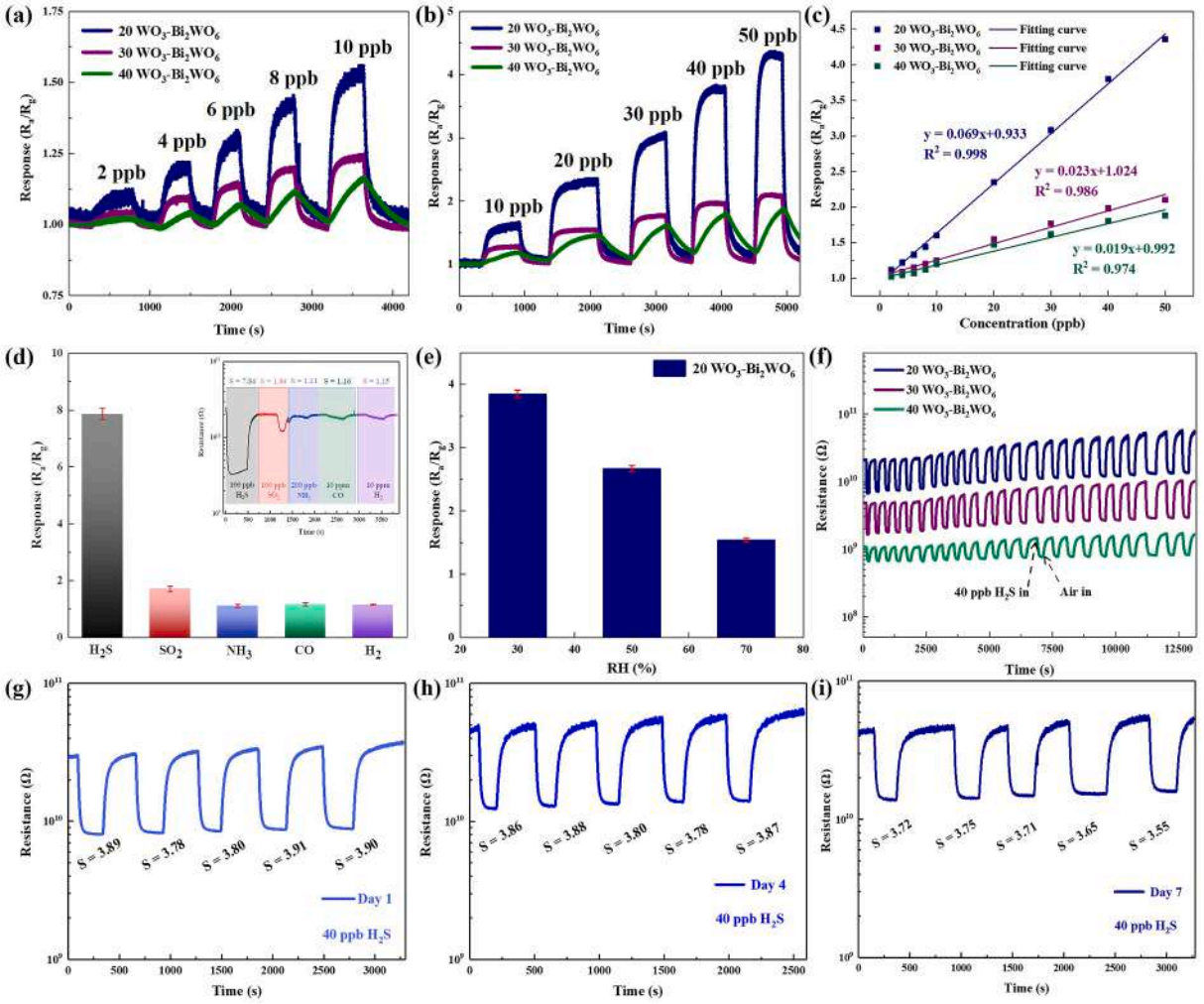

Fig. 5. (a, b) Dynamic sensing performance of 20 WO_3-Bi_2WO_6, 30 WO_3-Bi_2WO_6 and 40 WO_3-Bi_2WO_6 to 2–50 ppb H_2S at room temperature; (c) response values and the fitted curves of 20 WO_3-Bi_2WO_6, 30 WO_3-Bi_2WO_6 and 40 WO_3-Bi_2WO_6 versus H_2S concentration; (d) selectivity of 20 WO_3-Bi_2WO_6 to 100 ppb target gases at room temperature; (e) effect of relative humidity on 20 WO_3-Bi_2WO_6 to 40 ppb H_2S; (f) repeatable characteristics of 20 WO_3-Bi_2WO_6 in 24 consecutive responses; (g-i) repeatable characteristics of 20 WO_3-Bi_2WO_6 in day 1, day 4 and day 7.

was also be investigated. As shown in Fig. 5e, the response to 40 ppb H_2S is 3.86, 2.68 and 1.54, respectively. The dynamic resistance variations in various relative humidity are shown in Fig. S6. The decrease of both baseline resistance and response may be ascribed to the competition between water and oxygen molecules on the surface, resulting in less reaction of adsorbed oxygen and H_2S. To identify the repeatability of each sensor during continuous response-recovery cycles, we first measured the three effective gas sensors (20, 30, 40 WO_3-Bi_2WO_6) for ppb-level H_2S detection via controlling the gas concentration manually. The results during 24 cycles are shown in Fig. 5f, which demonstrate that the three sensors attained repeatable response in the continuous measurement to 40 ppb H_2S, moreover, it can be found the resistance variation of gas sensors did not decrease along with the testing time, so these sensors present promising and effective response to H_2S in the 24 cycles (the total testing time was around 13000 s). Furthermore, as for the best gas sensor, we test the stability of 20 WO_3-Bi_2WO_6 gas sensor during one week to 40 ppb H_2S at room temperature and relative humidity of around 30%. As shown in Fig. 5g–i, the response of 20 WO_3-Bi_2WO_6 towards 40 ppb H_2S in Day 1, 4 and 7 show good repeatability. The slight variation of response values to 40 ppb H_2S indicates that all the WO_3-Bi_2WO_6 composites gas sensors present a stable response at room temperature. Hence, the WO_3-Bi_2WO_6 composites gas sensors show expected performance in repeatability.

The comparison of hydrogen sulfide sensing properties between H_2S sensors in literature and 20 WO_3-Bi_2WO_6 sensor in this work is summarized in Table 1. Comparing with other Bi_2WO_6 based gas sensors, 20 WO_3-Bi_2WO_6 composite gas sensor presents significantly good room temperature H_2S sensing performance including higher response and faster response/recovery. Furthermore, compared with other metal oxide gas sensors in the literature, 20 WO_3-Bi_2WO_6 still exhibits the best H_2S sensing properties and the obvious advantage of low working temperature. Hence, it is a competitive room temperature H_2S sensor for practical application.

3.3. Gas sensing mechanism

As shown in Fig. 6, the response procedure, and the energy band diagram of WO_3-Bi_2WO_6 heterojunction after contact are used to explain the sensing mechanism of WO_3-Bi_2WO_6 gas sensors. The response process of WO_3-Bi_2WO_6 sensing material was explained via gas–solid phase reaction models [42,43]. As described in Fig. 6a and 6b, the surface adsorbed oxygen ($O_{2(ads)}$) will capture electrons from WO_3 and Bi_2WO_6 sensing materials to form $O_2^-{}_{(ads)}$ ions at a low working temperature. When the material detects H_2S gas, oxygen anions ($O_2^-{}_{(ads)}$) would oxidize H_2S molecules into water (H_2O) and sulfide dioxide (SO_2), as well as releasing electrons (e^-) back to the conduction band (CB) of WO_3 and Bi_2WO_6.

Table 1
H_2S sensing properties of metal oxides semiconductor sensors.

Materials	Working temp. (°C)	Concentration	Response (R_a/R_g)	$\tau_{res.}/\tau_{rec.}$	Refs.
Bi_2WO_6 nanostructure	260 °C	5 ppb	2.3	–	[23]
Bi_2WO_6/rGO	350 °C	250 ppb	2.7	~1000 s/350 s	[24]
Bi_2MoO_6 microflowers	170 °C	100 ppb	4.0	~80 s/500 s	[5]
$BiVO_4$porous film	75 °C	500 ppb	1.4	~150 s/40 s	[36]
$WO_3/Bi_2W_2O_9$ nanoflakes	92 °C	500 ppb	2.7	–	[37]
WO_3-SnO_2nanowires	200 °C	500 ppb	3.8	–	[38]
NiO/WO_3nanoparticles	100 °C	50 ppb	4.95 ± 2.9	–	[39]
WO_3/CuO	80 °C	300 ppb	2.14	~300 s/-	[40]
$ZnFe_2O_4$ nanofibers	350 °C	100 ppb	3.3	~160 s/210 s	[41]
20 WO_3-Bi_2WO_6	RT	50 ppb	4.4	52 s/119 s	This work

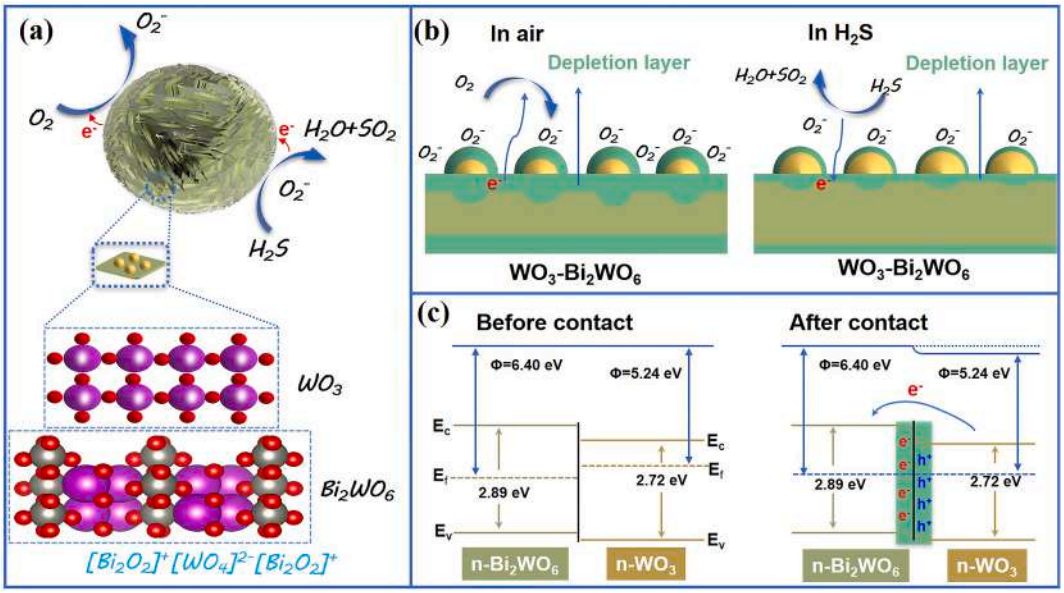

Fig. 6. (a, b) Schematic illustration of H_2S sensing mechanism for hierarchical WO_3-Bi_2WO_6 microflowers and (c) Energy band diagram of 20 WO_3-Bi_2WO_6 heterojunction structure.

$$O_{2\ (gas)} \rightarrow O_{2\ (ads)} \quad (1)$$

$$O_{2\ (ads)} + e^- \rightarrow O_2^-{}_{(ads)}\ (<150\ °C) \quad (2)$$

$$H_2S_{\ (gas)} \rightarrow H_2S_{\ (ads)} \quad (3)$$

$$2H_2S_{\ (ads)} + 3O_2^-{}_{(ads)} \leftrightarrow 2SO_2 + 2H_2O + 3e^-\ (25\ °C) \quad (4)$$

The enhancement mechanism is also proposed. First, it is acknowledged that the sensing ability of semiconductor material is dependent on the surface oxygen adsorb capability [44]. As confirmed from the BET results, WO_3-Bi_2WO_6 showed a larger specific surface area, which could provide more effective reaction regions and contribute to enhancing the sensing efficiency. But when the WO_3 amounts exceed 20 wt%, according to the BET results, the worse sensing performance may be caused by the overloaded WO_3 nanoparticles, and the effect of specific surface area might not play the dominant role. Second, the enhanced gas-sensing performance of WO_3-Bi_2WO_6 is closely attributed to the hierarchical and hollow microflowers. The hollow structure behaves in hierarchical and porous characteristics, providing enough gas transportation channels for H_2S molecules to diffuse into the WO_3-Bi_2WO_6 interior. Meanwhile, it also presents abundant active sites for the gas–solid phase reaction [45]. Thus, the sensing properties of WO_3-Bi_2WO_6 are improved. Third, it can be attributed to the difference in the energy level between n-type WO_3 nanoparticles (bandgap of ~ 2.72 eV) and n-type Bi_2WO_6 (bandgap of ~ 2.89 eV), as shown in Fig. 6c. After the two materials are contacted, electrons would flow from WO_3 to Bi_2WO_6 until reaching an equilibrium state of the Fermi levels. Meanwhile, the electrons are easily captured to generate more chemisorbed oxygen ions and there will form a wider electron depletion layer at the n-n heterojunction interface and an increased potential barrier height. Once the WO_3-Bi_2WO_6 sensor is exposed to H_2S, the oxidation reaction between chemisorbed oxygen ion and H_2S molecules will occur rapidly, resulting in an enhanced response [46]. Fourth, WO_3 when added in a high amount is no more effective in creating n-n heterojunction because the nanoparticles are too close together and shield the underneath Bi_2WO_6 phase.

3.4. Practicability of the 20 WO_3-Bi_2WO_6-based sensor

Monitoring the variation of H_2S concentration can serve as a rapid and non-destructive method for fish freshness assessment. The fresh fish (pangasius) was selected as the target object and monitoring the electrical resistance change of 20 WO_3-Bi_2WO_6 gas sensor during its spoilage process in 24 h at room temperature. Fig. 7a showed the correlation between sensor response values and various storage times at room temperature. The responses show a linear increase ($R^2 = 0.9922$) with the extension of dead fish storage time at 20 °C. Furthermore, the fabricated hierarchical 20 WO_3-Bi_2WO_6 microflowers sensor also displayed fine transient response characteristics towards the volatiles of fish fillet. In Fig. 7b, when 20 WO_3-Bi_2WO_6 gas sensor detected the released gases from the fish stored for 0, 12 and 24 h at 20 °C, the response values were 2.6, 6.2 and 10.7, respectively. This trend further

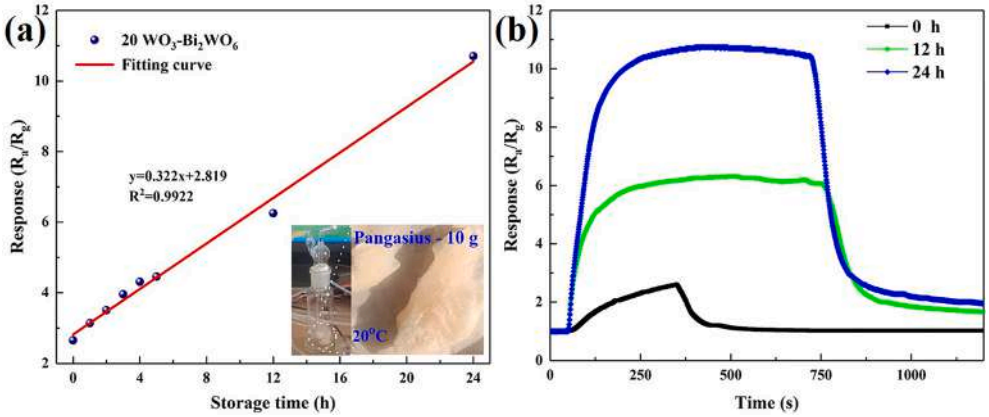

Fig. 7. (a) Responses of the 20 WO_3-Bi_2WO_6 sensor as a function of storage time measured at 20 °C under exposure to odors from pangasius, (b) response values of 20 WO_3-Bi_2WO_6 sensor to the volatiles from 10 g pangasius after storage for different times (0, 12, 24 h).

confirmed the obvious response changes of the sensor to different H_2S concentrations which were generated from the decomposition of sulfhydryl-containing amino acids during spoilage in pangasius [7].

4. Conclusion

Pristine Bi_2WO_6 nanosheets and hierarchical x wt% WO_3-Bi_2WO_6 (x = 10, 20, 30 and 40) microflowers were prepared via a facile hydrothermal technique. The loaded WO_3 nanoparticles modified the microstructure and morphology characteristics of WO_3-Bi_2WO_6 microflowers. WO_3 nanoparticles were loaded on the surface of hierarchical WO_3-Bi_2WO_6 microflowers assembled with thin nanosheets. The pristine Bi_2WO_6 and 10 WO_3-Bi_2WO_6 showed no response to H_2S whereas 20/30/40 WO_3-Bi_2WO_6 displayed improved sensing performance. Especially, 20 WO_3-Bi_2WO_6 microflowers showed the best sensing properties, including a high response value of 4.4 to 50 ppb H_2S, while that of 30/40 WO_3-Bi_2WO_6 were 2.0 and 1.9, respectively. The enhanced gas sensing properties may be ascribed to the catalytic effect of WO_3 nanoparticles, the modified hierarchical structure with a large specific surface area and the n–n heterojunction structure. 20 WO_3-Bi_2WO_6 microflowers gas sensor realizes the monitoring of fish freshness, which presents a rapid and high-sensitivity analysis towards the released gases of pangasius. Therefore, this work proposed a facile synthesis process to fabricate room temperature ppb-level H_2S gas sensors for non-destructive evaluating fish freshness and real-time monitoring environment.

Declaration of Competing Interest

The authors declare that they have no known competing financial interests or personal relationships that could have appeared to influence the work reported in this paper.

Acknowledgments

This work is supported by the Natural Science Foundation of China under Grant No. 51872254, the National Key Research and Development Program of China under Grant No. 2017YFE0115900, and the Outstanding Youth Foundation of Jiangsu Province of China under Grant No. BK20211548.

Appendix A. Supplementary data

Supplementary data to this article can be found online at https://doi.org/10.1016/j.cej.2021.132813.

References

[1] H. Luo, S. Chen, Z. Liu, C. Zhang, Z. Cai, X. Chen, G. Zhang, Y. Zhao, S. Decurtins, S.-X. Liu, D. Zhang, A cruciform electron donor-acceptor semiconductor with solid-state red emission: 1D/2D optical waveguides and highly sensitive/selective detection of H_2S gas, Adv. Funct. Mater. 24 (2014) 4250–4258, https://doi.org/10.1002/adfm.201304027.

[2] S. Ghosh, D. Adak, R. Bhattacharyya, N. Mukherjee, ZnO/γ-Fe_2O_3 charge transfer interface toward highly selective H_2S sensing at a low operating temperature of 30 °C, ACS Sens. 2 (2017) 1831–1838, https://doi.org/10.1021/acssensors.7b00636.

[3] F. Zhang, Y. Xu, X. Zhang, L. Sui, P. Hu, Z. Zheng, X. Cheng, S. Gao, H. Zhao, L. Huo, Highly selective ppb-level H_2S sensor based on the walnut-like Bi_2MoO_6 at low temperature, Sens. Actuators B Chem. 277 (2018) 312–319, https://doi.org/10.1016/j.snb.2018.08.151.

[4] Z. Jiang, J. Li, H. Aslan, Q. Li, Y. Li, M. Chen, Y. Huang, J.P. Froning, M. Otyepka, R. Zbořil, F. Besenbacher, M. Dong, A high efficiency H_2S gas sensor material: paper like Fe_2O_3/graphene nanosheets and structural alignment dependency of device efficiency, J Mater Chem A. 2 (2014) 6714–6717, https://doi.org/10.1039/C3TA15180H.

[5] X. Cui, Y. Xu, X. Zhang, X. Cheng, S. Gao, H. Zhao, L. Huo, In-situ deposited flower-like Bi_2MoO_6 microspheres thin film based sensors for highly selective detection of ppb-level H_2S at low temperature, Sens. Actuators B Chem. 247 (2017) 681–690, https://doi.org/10.1016/j.snb.2017.03.100.

[6] Y. Wang, G. Duan, Y. Zhu, H. Zhang, Z. Xu, Z. Dai, W. Cai, Room temperature H_2S gas sensing properties of In_2O_3 micro/nanostructured porous thin film and hydrolyzation-induced enhanced sensing mechanism, Sens. Actuators B Chem. 228 (2016) 74–84, https://doi.org/10.1016/j.snb.2016.01.002.

[7] B.-Y. Song, M. Zhang, Y. Teng, X.-F. Zhang, Z.-P. Deng, L.-H. Huo, S. Gao, Highly selective ppb-level H_2S sensor for spendable detection of exhaled biomarker and pork freshness at low temperature: Mesoporous SnO_2 hierarchical architectures derived from waste scallion root, Sens. Actuators B Chem. 307 (2020), 127662, https://doi.org/10.1016/j.snb.2020.127662.

[8] J.-H. Cha, D.-H. Kim, S.-J. Choi, W.-T. Koo, I.-D. Kim, Sub-parts-per-million hydrogen sulfide colorimetric sensor: Lead acetate anchored nanofibers toward halitosis diagnosis, Anal. Chem. 90 (2018) 8769–8775, https://doi.org/10.1021/acs.analchem.8b01273.

[9] J. Deng, J. Ma, L. Mei, Y. Tang, Y. Chen, T. Lv, Z. Xu, T. Wang, Porous α-Fe_2O_3 nanosphere-based H2S sensor with fast response, high selectivity and enhanced sensitivity, J. Mater. Chem. A. 1 (2013) 12400, https://doi.org/10.1039/c3ta12253k.

[10] F. Peng, Y. Sun, Y. Lu, W. Yu, M. Ge, J. Shi, R. Cong, J. Hao, N. Dai, Studies on Sensing Properties and Mechanism of CuO Nanoparticles to H_2S Gas, Nanomaterials. 10 (2020) 774, https://doi.org/10.3390/nano10040774.

[11] M. Wang, Q. Luo, S. Hussain, G. Liu, G. Qiao, E.J. Kim, Sharply-precipitated spherical assembly of ZnO nanosheets for low temperature H_2S gas sensing performances, Mater. Sci. Semicond. Process. 100 (2019) 283–289, https://doi.org/10.1016/j.mssp.2019.05.020.

[12] T.P. Mokoena, Z.P. Tshabalala, K.T. Hillie, H.C. Swart, D.E. Motaung, The blue luminescence of p-type NiO nanostructured material induced by defects: H_2S gas sensing characteristics at a relatively low operating temperature, Appl. Surf. Sci. 525 (2020), 146002, https://doi.org/10.1016/j.apsusc.2020.146002.

[13] K. Tian, X.-X. Wang, Z.-Y. Yu, H.-Y. Li, X. Guo, Hierarchical and hollow Fe_2O_3 nanoboxes derived from metal–organic frameworks with excellent sensitivity to H_2S, ACS Appl. Mater. Interfaces. 9 (2017) 29669–29676, https://doi.org/10.1021/acsami.7b07069.

[14] K. Wu, J. Xu, M. Debliquy, C. Zhang, Synthesis and NH_3/TMA sensing properties of $CuFe_2O_4$ hollow microspheres at low working temperature, Rare Met. 40 (2021) 1768–1777, https://doi.org/10.1007/s12598-020-01609-9.

[15] S.N. Shuvo, A.M. Ulloa Gomez, A. Mishra, W.Y. Chen, A.M. Dongare, L.A. Stanciu, Sulfur-doped titanium carbide MXenes for room-temperature gas sensing, ACS Sens. 5 (2020) 2915–2924, https://doi.org/10.1021/acssensors.0c01287.

[16] A. Mirzaei, S.S. Kim, H.W. Kim, Resistance-based H_2S gas sensors using metal oxide nanostructures: A review of recent advances, J. Hazard. Mater. 357 (2018) 314–331, https://doi.org/10.1016/j.jhazmat.2018.06.015.

[17] Y. Huan, K. Wu, C. Li, H. Liao, M. Debliquy, C. Zhang, Micro-nano structured functional coatings deposited by liquid plasma spraying, J. Adv. Ceram. 9 (2020) 517–534, https://doi.org/10.1007/s40145-020-0402-9.

[18] K. Wu, Y. Lu, Y. Liu, Y. Liu, M. Shen, M. Debliquy, C. Zhang, Synthesis and acetone sensing properties of copper (Cu^{2+}) substituted zinc ferrite hollow micro-nanospheres, Ceram. Int. 46 (2020) 28835–28843, https://doi.org/10.1016/j.ceramint.2020.08.049.

[19] X. Qiao, Y. Xu, K. Yang, J. Ma, C. Li, H. Wang, L. Jia, Mo doped $BiVO_4$ gas sensor with high sensitivity and selectivity towards H_2S, Chem. Eng. J. 395 (2020), 125144, https://doi.org/10.1016/j.cej.2020.125144.

[20] M. Punginsang, A. Wisitsoraat, A. Tuantranont, S. Phanichphant, C. Liewhiran, Ultrafine Bi_2WO_6 nanoparticles prepared by flame spray pyrolysis for selective acetone gas-sensing, Mater. Sci. Semicond. Process. 90 (2019) 263–275, https://doi.org/10.1016/j.mssp.2018.10.021.

[21] C. Li, G. Chen, J. Sun, J. Rao, Z. Han, Y. Hu, Y. Zhou, A novel mesoporous single-crystal-Like Bi_2WO_6 with enhanced photocatalytic activity for pollutants degradation and oxygen production, ACS Appl. Mater. Interfaces. 7 (2015) 25716–25724, https://doi.org/10.1021/acsami.5b06995.

[22] S. Adhikari, S. Selvaraj, D.-H. Kim, Construction of heterojunction photoelectrode via atomic layer deposition of Fe_2O_3 on Bi_2WO_6 for highly efficient photoelectrochemical sensing and degradation of tetracycline, Appl. Catal. B Environ. 244 (2019) 11–24, https://doi.org/10.1016/j.apcatb.2018.11.043.

[23] W. Liu, Y. Qu, H. Li, F. Ji, H. Dong, M. Wu, H. Chen, Z. Lin, Nanostructure Bi_2WO_6: Surfactant-assisted hydrothermal synthesis for high sensitive and selective sensing of H_2S, Sens. Actuators B Chem. 294 (2019) 224–230, https://doi.org/10.1016/j.snb.2019.05.042.

[24] K. Bunpang, A. Wisitsoraat, A. Tuantranont, S. Phanichphant, C. Liewhiran, Effects of reduced graphene oxide loading on gas-sensing characteristics of flame-made Bi_2WO_6 nanoparticles, Appl. Surf. Sci. 496 (2019), 143613, https://doi.org/10.1016/j.apsusc.2019.143613.

[25] J. Li, X. Liu, J. Cui, J. Sun, Hydrothermal synthesis of self-assembled hierarchical tungsten oxides hollow spheres and their gas sensing properties, ACS Appl. Mater. Interfaces. 7 (2015) 10108–10114, https://doi.org/10.1021/am508121p.

[26] H. Huang, R. Cao, S. Yu, K. Xu, W. Hao, Y. Wang, F. Dong, T. Zhang, Y. Zhang, Single-unit-cell layer established Bi_2WO_6 3D hierarchical architectures: Efficient adsorption, photocatalysis and dye-sensitized photoelectrochemical performance, Appl. Catal. B Environ. 219 (2017) 526–537, https://doi.org/10.1016/j.apcatb.2017.07.084.

[27] D. He, L. Wang, D. Xu, J. Zhai, D. Wang, T. Xie, Investigation of photocatalytic activities over Bi_2WO_6/$ZnWO_4$ composite under UV light and its photoinduced charge transfer properties, ACS Appl. Mater. Interfaces. 3 (2011) 3167–3171, https://doi.org/10.1021/am200664y.

[28] Q. Zhou, Y. Song, N. Li, D. Chen, Q. Xu, H. Li, J. He, J. Lu, Direct Dual Z-Scheme Bi_2WO_6 /GQDs/WO_3 inverse opals for enhanced photocatalytic activities under visible light, ACS Sustain. Chem. Eng. 8 (2020) 7921–7927, https://doi.org/10.1021/acssuschemeng.0c01548.

[29] X. Chen, Y. Li, L. Li, Facet-engineered surface and interface design of WO_3/Bi_2WO_6 photocatalyst with direct Z-scheme heterojunction for efficient salicylic acid removal, Appl. Surf. Sci. 508 (2020), 144796, https://doi.org/10.1016/j.apsusc.2019.144796.

[30] M. Zhang, C. Lai, B. Li, D. Huang, S. Liu, L. Qin, H. Yi, Y. Fu, F. Xu, M. Li, L. Li, Ultrathin oxygen-vacancy abundant WO_3 decorated monolayer Bi_2WO_6 nanosheet: A 2D/2D heterojunction for the degradation of Ciprofloxacin under visible and NIR light irradiation, J. Colloid Interface Sci. 556 (2019) 557–567, https://doi.org/10.1016/j.jcis.2019.08.101.

[31] Z. Li, M. Luo, B. Li, Q. Lin, X. Liao, H. Yu, C. Yu, 3-D hierarchical micro/nano-structures of porous Bi_2WO_6: Controlled hydrothermal synthesis and enhanced photocatalytic performances, Microporous Mesoporous Mater. (2020), 110830, https://doi.org/10.1016/j.micromeso.2020.110830.

[32] H. Zhou, Z. Wen, J. Liu, J. Ke, X. Duan, S. Wang, Z-scheme plasmonic Ag decorated WO_3/Bi_2WO_6 hybrids for enhanced photocatalytic abatement of chlorinated-VOCs under solar light irradiation, Appl. Catal. B Environ. 242 (2019) 76–84, https://doi.org/10.1016/j.apcatb.2018.09.090.

[33] Y. Su, B. Zhu, K. Guan, S. Gao, L. Lv, C. Du, L. Peng, L. Hou, X. Wang, Particle size and structural control of $ZnWO_4$ nanocrystals via Sn^{2+} doping for tunable optical and visible photocatalytic properties, J. Phys. Chem. C. 116 (2012) 18508–18517, https://doi.org/10.1021/jp3052505.

[34] P.M. Bulemo, H.-J. Cho, N.-H. Kim, I.-D. Kim, Mesoporous SnO_2 nanotubes via electrospinning–etching route: Highly sensitive and selective detection of H_2S molecule, ACS Appl. Mater. Interfaces. 9 (2017) 26304–26313, https://doi.org/10.1021/acsami.7b05241.

[35] D. Meng, D. Liu, G. Wang, Y. Shen, X. San, M. Li, F. Meng, Low-temperature formaldehyde gas sensors based on NiO-SnO_2 heterojunction microflowers assembled by thin porous nanosheets, Sens. Actuators B Chem. 273 (2018) 418–428, https://doi.org/10.1016/j.snb.2018.06.030.

[36] C. Li, X. Qiao, J. Jian, F. Feng, H. Wang, L. Jia, Ordered porous $BiVO_4$ based gas sensors with high selectivity and fast-response towards H_2S, Chem. Eng. J. 375 (2019), 121924, https://doi.org/10.1016/j.cej.2019.121924.

[37] Y. Zhang, X. Zhang, C. Guo, Y. Xu, X. Cheng, F. Zhang, Z. Major, L. Huo, Novel two-dimensional WO_3/$Bi_2W_2O_9$ nanocomposites for rapid H_2S detection at low temperatures, ACS Appl. Mater. Interfaces. 12 (2020) 54946–54954, https://doi.org/10.1021/acsami.0c15611.

[38] T.T.N. Hoa, D.T.T. Le, N. Van Toan, N. Van Duy, C.M. Hung, N. Van Hieu, N. D. Hoa, Highly selective H_2S gas sensor based on WO_3-coated SnO_2 nanowires, Mater. Today Commun. 26 (2021), 102094, https://doi.org/10.1016/j.mtcomm.2021.102094.

[39] D. Feng, L. Du, X. Xing, C. Wang, J. Chen, Z. Zhu, Y. Tian, D. Yang, Highly Sensitive and selective NiO/WO_3 composite nanoparticles in detecting H_2S biomarker of halitosis, ACS Sens. 6 (2021) 733–741, https://doi.org/10.1021/acssensors.0c01280.

[40] M. He, L. Xie, X. Zhao, X. Hu, S. Li, Z.-G. Zhu, Highly sensitive and selective H_2S gas sensors based on flower-like WO_3/CuO composites operating at low/room temperature, J. Alloys Compd. 788 (2019) 36–43, https://doi.org/10.1016/j.jallcom.2019.01.349.

[41] N. Van Hoang, C.M. Hung, N.D. Hoa, N. Van Duy, N. Van Hieu, Facile on-chip electrospinning of $ZnFe_2O_4$ nanofiber sensors with excellent sensing performance to H_2S down ppb level, J. Hazard. Mater. 360 (2018) 6–16, https://doi.org/10.1016/j.jhazmat.2018.07.084.

[42] Z. Wu, Z. Li, H. Li, M. Sun, S. Han, C. Cai, W. Shen, Y. Fu, Ultrafast response/recovery and High selectivity of the H_2S gas sensor based on α-Fe_2O_3 nano-ellipsoids from one-step hydrothermal synthesis, ACS Appl. Mater. Interfaces. 11 (2019) 12761–12769, https://doi.org/10.1021/acsami.8b22517.

[43] L. Sui, T. Yu, D. Zhao, X. Cheng, X. Zhang, P. Wang, Y. Xu, S. Gao, H. Zhao, Y. Gao, L. Huo, In situ deposited hierarchical CuO/NiO nanowall arrays film sensor with enhanced gas sensing performance to H_2S, J. Hazard. Mater. 385 (2020), 121570, https://doi.org/10.1016/j.jhazmat.2019.121570.

[44] J. Miao, C. Chen, L. Meng, Y.S. Lin, Self-assembled monolayer of metal oxide nanosheet and structure and gas-sensing property relationship, ACS Sens. 4 (2019) 1279–1290, https://doi.org/10.1021/acssensors.9b00162.

[45] C. Zhang, D. Sun, Y. Huan, K. Wu, H. Liao, Highly sensitive ZnO nanoparticles-loaded In_2O_3 hollow microsphere for detecting ppb-level NO_2 at low working temperature, Prog. Nat. Sci. Mater. Int. 30 (2020) 469–476, https://doi.org/10.1016/j.pnsc.2020.06.006.

[46] D. Zhang, C. Jiang, J. Wu, Layer-by-layer assembled In_2O_3 nanocubes/flower-like MoS_2 nanofilm for room temperature formaldehyde sensing, Sens. Actuators B Chem. 273 (2018) 176–184, https://doi.org/10.1016/j.snb.2018.06.044.